The high sensitivity of InN under rare earth ion implantation at medium range energy

B Lacroix[1], M P Chauvat[1], P Ruterana[1], K Lorenz[2], E Alves[2] and A Syrkin[3]

[1] Centre de Recherche sur les Ions, les Matériaux et la Photonique, UMR 6252 CNRS-ENSICAEN-CEA-UCBN, 6, Boulevard du Maréchal Juin, 14050 Caen Cedex, France

[2] Instituto Tecnológico e Nuclear, EN 10, 2686-953 Sacavém, Portugal

[3] Technologies and Devices International, an Oxford Instruments Company, 12214 Plum Orchard Dr. Silver Spring, MD 20904, USA

Abstract

In this work, the damage formation in InN layers has been investigated subsequent to europium implantation at 300 keV and room temperature. The layers of several microns were produced by Hydride Vapour Phase Epitaxy and used as matrices for ion implantation experiments due to their good crystalline quality. From this investigation, it is shown that InN exhibits a low stability under rare earth ion implantation. Starting at a low fluence of around $5x10^{12}$ Eu/cm^2, an extensive modification of the surface layer takes place. The dissociation of InN and the presence of misoriented nanograins are observed in the damaged area. Analysis by electron diffraction indicates that the nanograins correspond to indium oxide In_2O_3.

Keywords: InN, ion implantation, TEM, rare earth

I. Introduction

For the last two decades, the group of III-V nitride semiconductors (AlN, GaN and InN) has been intensively investigated owing to their high technological application potential in micro- and opto-electronics [1,2]. In the semiconductor technology, ion implantation is extensively used to tune the properties and functionalities of materials. It offers a wide range of energies and constitutes an interesting tool to perform dry etching, ion cut, electrical isolation, and to introduce electrically and optically active dopants below the surface. In particular, for gallium nitride, ion implantation at medium range energy (one to a few hundred keV) has attracted much attention to investigate the n or p doping with Si or Mg species, but also to incorporate optically active rare earth elements [3,4]. Thus, the literature about ion implantation and correlated irradiation effects on GaN is becoming more and more complete [5-7]. In particular, the mechanisms of damage formation have been shown to differ from the conventional scheme of amorphization [8-11]. In the case of AlN, only a few reports are available on electronic quality layers, as was shown, this material is resistant to ion implantation damage formation and the amorphization has been shown to take place at very high implantation fluences (~10^{17} at./cm^2) [12]. As for InN, despite its potential practical importance, data on the effect of ion implantation and irradiation are still scarce. During the last decade, important advances have been made on InN growth, and its band gap has been redefined from the earlier of 1.89 eV to 0.67 eV using layers grown by molecular beam epitaxy [13,14] where layers thickness of up to 10 µm have been grown [15]. Up to now, successful growth has also been reported by metalorganic vapour phase epitaxy [16,17] and the highest rates for this substantially low temperature growth material is now achieved by hydride vapor phase epitaxy (HVPE), where some 4µm/h growth rates can be obtained around 500°C [18]. In the following, we report on the investigation of the damage formation in HVPE InN layers subsequent to Eu ion implantation at 300 keV. In contrast to GaN and AlN,

where highly efficient dynamic annealing has been reported [3,5] and severe damage in form of nanocrystallization (GaN) [9-11] or amorphization (AlN) [12] occurs only at substantially higher fluences, it is shown that the implantation of these heavy rare earth ions, strongly damages InN at very low fluences, starting in the 10^{12} at./cm^2 range.

II. Experimental

Indium nitride (InN) was grown on a (0001) gallium nitride (GaN) buffer layer deposited on (0001) sapphire by hydride vapor phase epitaxy. InN was then implanted at room temperature with europium (Eu) ions at 300 keV. The mean projected range, *Rp*, the straggling, *ΔRp*, and the position of the maximum of damage from the surface are 60 nm, 24 nm, and 38 nm, respectively (using Monte-Carlo SRIM calculations [19]). Structural investigations were conducted through transmission electron microscopy (TEM) experiments. Cross-section samples were thinned down to less than 10 µm by mechanical polishing using the tripod method. The electron transparency was achieved by ion milling at 5 kV using the GATAN precision ion polisher system (PIPS) at an incidence angle of 5° with the sample holder kept at 150K in order to minimize the beam damage to the samples. Observations were carried out by conventional and high resolution transmission electron microscopy in JEOL 2010 (CTEM) and JEOL 2010F (HRTEM) microscopes operated at 200 keV.

III. Results

In order to determine the TEM sample preparation effects on the InN layer structure, we have first made observations on a reference InN layer, from the same wafer, which has not undergone ion implantation. Its microstructure is shown in figure 1. As can be noticed, the InN layer has a relatively large surface roughness with a peak to peak extension of about 100 nm. The dislocations which have a *c* character slightly bend at the InN/GaN interface and

cross the InN layer to the surface as shown in the **g**=0002 weak beam image of figure 1(a). The **g**=$1\bar{1}00$ weak beam image of the same area shows other interesting features (figure 1(b)). As can be seen, most of the threading dislocations in the GaN buffer layer are of mixed type $1/3<11\bar{2}3>$. Moreover, the surface morphology appears to be connected to new networks of edge and mixed type dislocations which have been generated at the InN/GaN interface. This contrast in figure 1(b) is clearly indicative of domain growth with various small rotations around the *c* axis [20] from mosaic growth of InN on GaN which have large differences in *a* parameter. Each domain contains a high density of basal stacking faults (BSFs) which extend until the surface. This is in contrast to the growth of GaN where the SFs are mainly localized close to the interface with the sapphire substrate [21]. In the case of InN, the SFs extension towards the surface is mediated by prismatic stacking faults (PSFs) [22,23] which are also in contrast with **g**=$1\bar{1}00$ (figure 1(b)).

After implantation at $5x10^{12}$ Eu/cm^2, the surface layer of the wafer is dramatically modified to a depth of around 110 to 130 nm (figure 2). In the dark field images acquired with **g**=0002 (figure 2(a)) and **g**=$1\bar{1}00$ (figure 2(b)), the highly damaged areas exhibits three different contrasts as have been labelled A, B and C. The B layer, which corresponds to the highest concentration of the damage, exhibits a dark contrast and follows, as would be expected, the surface morphology. This dark buried layer is centred on *Rp* and it is embedded between the bright A and C areas which are defective but exhibit a monocrystalline contrast. As can be noticed by comparing figure 1 and figure 2, the defects which were observed immediately after the growth all along the InN layer (dislocations and SFs) are now interrupted by the damaged layer formed during implantation at the initiation of layer B.

As shown along the $[11\bar{2}0]$ zone axis micrograph of figure 3, the B area structure completely differs from A and C. It contains bright and dark contrasts of various shapes and extensions (their lateral size can reach 30 to 50 nm). The HRTEM images acquired in the implanted layer

(figure 4(a) and figure 4(b)) reveal that: (i) the A region at the surface is crystalline, (ii) the B layer is highly damaged and it contains small misoriented nanograins surrounded by large bright areas which could be ascribed either to amorphous pockets, voids or N_2 gas bubbles due to InN dissociation. We can notice the presence of Moiré fringes (labelled *m*) in the B layer which indicate the overlap of grains with different orientations. The corresponding diffraction pattern is displayed in figure 5(a): it contains both spots of InN and additional coarser and distorted spots whose positions do not match perfectly with the InN wurtzite structure (see for example the S_1, S_2, S_3, S_4, S_5, S_6 and S_7 spots indicated by white arrows). These extra spots might have various origins: (i) Are they related to less stable InN polytypes such as the zinc-blende phase or the high pressure rocksalt structure? (ii) Can they be ascribed to the formation of metallic In due to the In-N dissociation? (iii) Can they be related to indium oxide (In_2O_3) subsequent to the oxidation of metallic In when the sample is removed from the implantation chamber, as was previously proposed by Timmers *et al.* [24]? To check these assumptions, powder diffraction patterns of the above structures have been simulated using the JEMS software [25] and compared to the experimental SAED pattern which was acquired close to the interface between the implanted and the non-implanted layer, in order to get a reliable reference from the undamaged InN crystal.

As would be expected, all the fine spots observed on the diffraction pattern are related to the InN wurtzite structure. However, this phase as well as the pure metallic In tetragonal phase or the InN rocksalt structure are not able to describe satisfactorily the coarse and distorted spots indicated by S_1, S_2, S_3, S_4 and S_5 (simulations not shown here). The simulations of the cubic InN zinc-blende and the In_2O_3 structures lead to a better description of the diffraction pattern: the S_1, S_2, S_4 and S_5 spots can be related to the (111), $(1\bar{1}1)$, (002) and (220) reflections of the InN zinc-blende phase, and/or to the (222), $(22\bar{2})$, (004) and (440) reflections of In_2O_3, respectively, both structures being viewed along the $[\bar{1}10]$ zone axis. Moreover, the angles

between these spots are consistent with the cubic symmetry: for example, for cubic In_2O_3 the angle relationship between the (222) planes and the $(22\bar{2})$, (004) and (440) are about 70°, 55° and 35°, respectively. Nevertheless, the S_3 weak spot, which is inclined by 90° from the S_1 spot, but also the S_6 and S_7 can only be identified as the $(\bar{1}\bar{1}2)$, (226) and $(\bar{2}\bar{2}6)$ reflections of In_2O_3. Obviously, by symmetry, the grains rotate by 70° around the $[\bar{1}10]$ zone axis to keep the other {111} planes parallel to the surface, but also the in-plane grains rotation by 180° enable to fully explain the presence of the other spots in figure 5(b). Therefore, the very good agreement between simulated and experimental diffraction patterns shows that cubic In_2O_3 is present in the implanted area.

To localize the different phases which have been identified above, a detailed HRTEM analysis of the near surface image (Fig 4(a)) was performed (not shown here). By filtering the Fourier image with specific spots, this study indicates that the crystalline A region may correspond to a wurtzite phase, whereas the small misoriented nanograins in the B layer are related to the InN zinc-blende and the In_2O_3 bixbyite structures. Rutherford backscattering spectrometry measurements (not shown) on the same implanted layers furthermore show a strong change in stochiometry within the implanted region in agreement with the existence of In_2O_3 and confirming that the observed results are not caused by the TEM sample preparation.

IV. Discussion

This work clearly shows that InN is very sensitive to the damage induced by the rare earth ion beam at medium range energy. A high degree of disorder is observed close to the surface after implantation at very low fluence ($5x10^{12}$ Eu/cm^2), within a layer of about 110 to 130 nm in width: while the first 10 to 20 nm remain crystalline, the underlying layer exhibits a much more complex microstructure. The latter is composed of small misoriented nanograins whose structure is shown to be different from InN. Within this detailed investigation of the electron

diffraction patterns, we have been able to extract more information about the structure of these nanograins. The simulations of the most probable expected phases indicate that those grains exhibit the In_2O_3 bixbyite structure. Moreover, in the highly damaged layer, large bright areas have formed and they can be identified either as amorphous pockets, voids or N_2 gas bubbles resulting from the dissociation of InN (breaking of the In-N bonds). Significant nitrogen depletion in InN was previously observed by different authors after irradiation, implantation or ion beam analysis experiments [26-29] but also after annealing at around 550°C [30]. Thus, in our case, a nitrogen release seems to be the most probable phenomenon. This nitrogen loss should be accompanied by a stoichiometry modification, which is in contradiction with the assumption of a wurtzite to zinc-blende phase transformation. Instead, InN dissociation could explain the presence of indium oxide nanograins in the N-depleted region. It may be expected that an important N depletion leads to the formation of metallic In clusters. Then, as proposed in Ref. [24], oxidation of the metallic In phase could occur when the sample is removed from the implantation chamber to air. Indeed, because the heat formation at room temperature of In_2O_3 (-221.27 kcal/mol) is significantly lower than InN (-4.2 kcal/mol) [31], indium would exhibit a stronger preference to the oxidation process.

During rare earth implantation in the same conditions, the fluence range leading to the breakdown of the wurtzite structure of GaN and AlN is about three to five orders of magnitude higher than for InN, and it was shown that the damage build-up is driven by the formation of a dense network of extended defects (mainly basal stacking faults). For GaN, the formation of a nanocrystalline layer from the surface occurs above $2x10^{15}$ Eu/cm^2, when the stacking fault network has reached the surface [10,11]. For AlN, the stacking fault network does not reach the surface and an amorphization in the bulk, around *Rp*, has been reported for fluences higher than 10^{17} Eu/cm^2 [12].

The high resistance to amorphization of GaN and AlN has been ascribed to an efficient dynamic annealing during implantation [32,33] which enables the defect annihilation and the arrangement into an array of planar defects. In absence of dynamic annealing, the damage accumulation leads to a complete lattice disordering or to amorphization when each atom has been moved approximately one time (1 displacement per atom (dpa)). For example, amorphization in silicon was reported at a fluence of $7x10^{13}$ Eu/cm^2 after implantation at 300 keV and RT at a maximum of damage close to 0.8 dpa [34].

In an attempt to explain this behaviour, we also carried out SRIM calculations of the damage and ion profiles for the implantation at $5x10^{12}$ Eu/cm^2 and 300 keV. In their report on this material, Mkhoyan and Silcox [27] pointed out that InN, with its cohesive energy per bond of about 1.9 eV, should have a surface binding energy between 5-6 eV and its bulk displacement energy should be approximately five times higher. So, displacement energies (E_d) of 25 eV for both In and N were used, and this led to very low calculated values of 0.05 dpa and 0.001 % atomic fraction, respectively. This maximum of damage (0.05 dpa) is far from 1 dpa which may indicate that the structural breakdown of InN is probably not dominated by nuclear interactions (ballistic collisions).

In their work on InGaN alloys, Kucheyev *et al.* [33] pointed out the detrimental effect of indium on the structure stability, and they showed that an increase of the In content degrades the dynamic annealing efficiency during the ion implantation. They related the lower dynamic annealing efficiency of the III-N semiconductors containing indium to the lower In-N binding energy, in comparison with the Ga-N or Al-N binding energies. For InN, GaN and AlN, the cohesive energies (E_c) are E_c^{InN} =7.970 eV/atom, E_c^{GaN} =9.058 eV/atom and E_c^{AlN} =11.669 eV/atom, respectively: these values correspond to experimental data reported in Ref. [35], and then reported after correction by phonon zero-point energies and by atomic spin-orbit splitting in Refs. [36-37]. In addition to the energetic aspect of the atomic bonds, it is also particularly

interesting to consider the formation enthalpies of these III-N semiconductors, which bring essential information about their thermodynamical stability. Indeed, by comparison with AlN and GaN, the wurtzite structure of InN exhibits a significantly lower formation enthalpy (ΔH_f), of about one range of magnitude (ΔH_f^{InN} =-0.21 eV, ΔH_f^{GaN} =-1.08 eV and ΔH_f^{AlN} =-3.13 eV) [38] which means that InN is not as stable as GaN or AlN. Several studies have also been devoted to the calculations of the cohesive energies and the formation enthalpies of the nitride semiconductors. In particular, Zoroddu *et al.* [37] have performed density-functional calculations, using the LDA and GGA methods, to predict the physical properties (values from the literature are reported in Table II). For the III-V nitrides, the calculations concluded to a stable wurtzite structure as experimentally observed, and it was shown that the GGA method led to a better agreement with the experimental results than LDA for AlN and GaN. The same authors also calculated the formation enthalpies and reported a very good match with experiments for AlN and GaN using the GGA. However, surprisingly, the GGA calculations of ΔH_f for InN gave a small but positive value which led the authors to conclude that InN may be thermodynamically unstable [37].

V. Conclusion

From the above observations, it is clear that InN is not stable during rare earth implantation at very low fluences ($5x10^{12}$ Eu/cm^2). Interestingly, the damage formation follows a conventional distribution and the crystalline system breaks down around *Rp*, where the concentration of implanted ion is the highest and where the largest part of atomic displacements occurs. In the damaged area, both InN dissociation and presence of indium oxide nanograins are evidenced. From the SRIM simulations, these fluences correspond to negligible displacements (0.05 dpa) and very low rare earth concentrations (0.001%). This is

an indication that the ballistic effects may not be dominant and it points to the fact that indium nitride may exhibits an intrinsic metastable character, as appears to have been deduced from previous GGA calculations. These results need now to be confirmed, and in particular, *in situ* experiments are in progress in order to determine the origin of the observed In_2O_3.

Acknowledgment

The authors acknowledge the support of the 'Région Basse Normandie' and of FCT Portugal (Ciência 2007 and PTDC/CTM/100756/2008) to this research work.

References

[1] Nakamura S and Fasol G 2000 *The Blue Laser Diode* (Springer, New York)

[2] Morkoc H 2008 *Handbook of Nitride Semiconductors and Devices* vol. 3 (Wiley-VcH, Berlin)

[3] Pearton S J, Ren F, Zhang A P and Lee K P 2000 *Mater. Sci. Eng.* R. **30** 55

[4] Mamor M, Matias V, Vantomme A, Colder A, Marie P and Ruterana P 2004 *Appl. Phys. Lett.* **85** 2244

[5] Kucheyev S O, Williams J S, Jagadish C, Zou J, and Li G 2000 *Phys. Rev. B* **62** 7510

[6] Lorenz K, Barradas N P, Alves E, Roqan S, Nogales E, Martin R W, O'Donnell K P, Gloux F and Ruterana P 2009 *J. Phys. D Appl. Phys.* **42** 165103

[7] Kucheyev S O, Williams J S and Pearton S J 2001 *Mater. Sci. Eng.* R **33** 51

[8] Ding F-R, He W-H, Vantomme A, Zhao Q, Pipeleers B, Jacobs K and Moerman I 2003 *Mat. Sci. Semicon. Processing* **5** 511

[9] Bae I T, Jiang W, Wang C, Weber W J and Zhang Y 2009 *J. Appl. Phys.* **105** 83514

[10] Gloux F, Wojtowicz T, Ruterana P, Lorenz K and Alves E 2006 *J. Appl. Phys.* **100** 073520

[11] Ruterana P, Lacroix B and Lorenz K 2011 *J. Appl. Phys.* **109** 013506

[12] Lorenz K, Alves E, Gloux F, Ruterana P, Peres M, Neves A J and Monteiro T 2010 *J. Appl. Phys.* **107** 023525

[13] Davydov V Y *et al.* 2002 *Phys. Stat. Sol. (b)* **230** R4

[14] Davydov V Y *et al.* 2002 *Phys. Stat. Sol. (b)* **234**, 787

[15] Liu B *et al.* 2008 *J. Appl. Phys.* **103** 23540

[16] Ruterana P, Abouzaid M, Gloux F, Maciej M, Doualan J L, Drago M, Schmidtling T, Pohl U W and Richter W 2006 *Phys. Stat. Sol. (a)* **203** 158

[17] Lozano J G, Sánchez A M, García R, Gonzalez D, Briot O and Ruffenach S 2006 *Appl. Phys. Lett.* **88**, 151913

[18] Ruterana P, Syrkin A L, Monroy E, Valcheva E and Kirilov K 2010 *Phys. Stat. Sol. (c)* **7** 1301

[19] Ziegler J F, Biersack J P and Littmark U 1985 *The Stopping and Range of Ions in Solids* (Pergamon, New York)

[20] Potin V, Ruterana P, Nouet G, Pond R C and Morkoç H 2000 *Phys. Rev. B* **61** 5587

[21] Potin V, Ruterana P and G. Nouet 2000 *J. Phys.: Condens. Matter*. **12** 10301

[22] Potin V, Vermaut P, Ruterana P and Nouet G 1998 *J. Electron. Mater.* **27** 266

[23] Vermaut P, Nouet G and Ruterana P 1999 *Appl. Phys Lett.* **74** 694

[24] Timmers H, Shrestha S K and Byrne A P 2004 *J. Cryst. Growth* **269** 50

[25] Stadelmann P A 1987 *Ultramicroscopy* **21** 131

[26] Emtsev V V, Davydov V Y, Haller E E, Klochikhin A A, Kozlovskii V V, Oganesyan G A, Poloskin D S, Shmidt N M, Vekshin V A and Usikov A S 2001 *Physica B: Condens. Matter* **308-310** 58

[27] Mkhoyan K A and Silcox J 2003 *Appl. Phys. Lett.* **82** 859

[28] Kosiba R, Ecke G, Cimalla V, Spie L, Krischok S, Schaefer J A, Ambacher O and Schaff W J 2004 *Nucl. Instrum. Methods B* **215** 486

[29] Shrestha S K, Timmers H, Butcher K S A, Wintrebert-Fouquet M and Chen P P-T 2005 *Nucl. Instrum. Methods B* **234** 291

[30] Guo Q, Kato O and Yoshida A 1993 *J. Appl. Phys.* **73** 7969

[31] Weast R C 1983-1984 *CRC Handbook of Chemistry and Physics* (Florida: Academic)

[32] Williams J S 1998 *Mater. Sci. Eng. A* **253** 8

[33] Kucheyev S O, Williams J S, Zou J and Jagadish C 2004 *J. Appl. Phys.* **95** 3048

[34] Gloux F, Ruterana P, Lorenz K and Alves E 2008 *Phys. Stat. Sol. (a)* **205** 68

[35] Harrison W A 1989 *Electronic Structure and the Properties of Solids* (Dover, New York)

[36] Paulus B, Shi F -H and Stoll H 1997 *J. Phys. Condens. Matter* **9** 2745

[37] Zoroddu A, Bernardini F, Ruggerone P and Fiorentini V 2001 *Phys. Rev. B* **64**, 045208

[38] Parsons R 1967 *D'Ans-Lax Taschenbuch für Chemiker und Physiker*, Band I, ed E Lax and C Synowietz (Springer, Berlin)

[39] Bhuiyan A G, Hashimoto A and Yamamoto A 2003 *J. Appl. Phys.* **94** 2779

[40] Serrano J, Rubio A, Hernandez E, Munoz A and Mujica A 2000 *Phys. Rev. B* **62** 16612

[41] Smith J and Schneider V 1964 *J. Less Common Met.* **7** 17

[42] Fuchs F and Bechstedt F 2008 *Phys. Rev. B* **77** 155107

TABLES

Phase	Symmetry (Structure type)	Space group	Lattice parameter (Å)	Ref.
InN	Hexagonal (Wurtzite)	P63mc	a=b=3.5365 c=5.7039	[39]
InN	Cubic (Zinc-Blende)	$F\bar{4}3m$	a=4.98	[39]
InN	Cubic (Rocksalt)	$Fm\bar{3}m$	a=4.636	[40]
In	Tetragonal	I4/mmm	a=b=4.5912 c=4.9355	[41]
In_2O_3	Cubic (Bixbyite)	$Ia\bar{3}$	a=10.094	[42]

TABLE I. Structural parameters used for powder diffraction simulations of the different expected phases in the damaged layer.

		AlN	GaN	InN
E_c (eV/atom)	Exp.	11.669	9.058	7.970
	Calc. (LDA)	13.536	10.999	9.249
	Calc. (GGA)	12.071	9.265	7.695
ΔH_f (eV)	Exp.	-3.13	-1.08	-0.21
	Calc. (LDA)	-3.642	-1.685	-0.303
	Calc. (GGA)	-3.142	-1.102	0.125

TABLE II. Cohesive energy, E_c, and formation enthalpy, ΔH_f, for wurtzite AlN, GaN and InN, from Refs. [36-38].

Figures captions

FIG. 1. Cross-section view of the as-grown InN layer using (a) **g**=0002 and (b) **g**=$1\bar{1}00$ weak beam conditions.

FIG. 2. Cross-section view of the InN layer after Eu implantation at $5x10^{12}$ Eu/cm^2 using (a) **g**=0002 and (b) **g**=$1\bar{1}00$ weak beam conditions.

FIG. 3. Cross-section view of the InN layer, viewed along the $[11\bar{2}0]$ zone axis, after Eu implantation at $5x10^{12}$ Eu/cm^2. Bright areas of various shape and size are evidenced in the damaged area.

FIG. 4. HRTEM performed along the $[11\bar{2}0]$ zone axis of InN in the implanted region after $5x10^{12}$ Eu/cm^2 implantation, (a) close to the surface and (b) in the highly damaged layer. Moiré fringes, labelled by *m*, are visible.

FIG. 5. Diffraction patterns of the damaged area of InN, after Eu implantation. (a) Some unexpected and unidentified spots (S_1, S_2, S_3, S_4, S_5, S_6 and S_7) are indicated by white arrows on the experimental diffraction pattern. (b) Simulation of the diffraction pattern of cubic (bixbyite) structure of In_2O_3. The dotted rings correspond to the most intense reflections. Some new spots are identified with respect to the $[\bar{1}10]$ zone axis, with the (111) planes parallel to the surface. The other spots are easily deduced by 70° rotation around $[\bar{1}10]$ to keep the other {111} planes parallel to the surface.

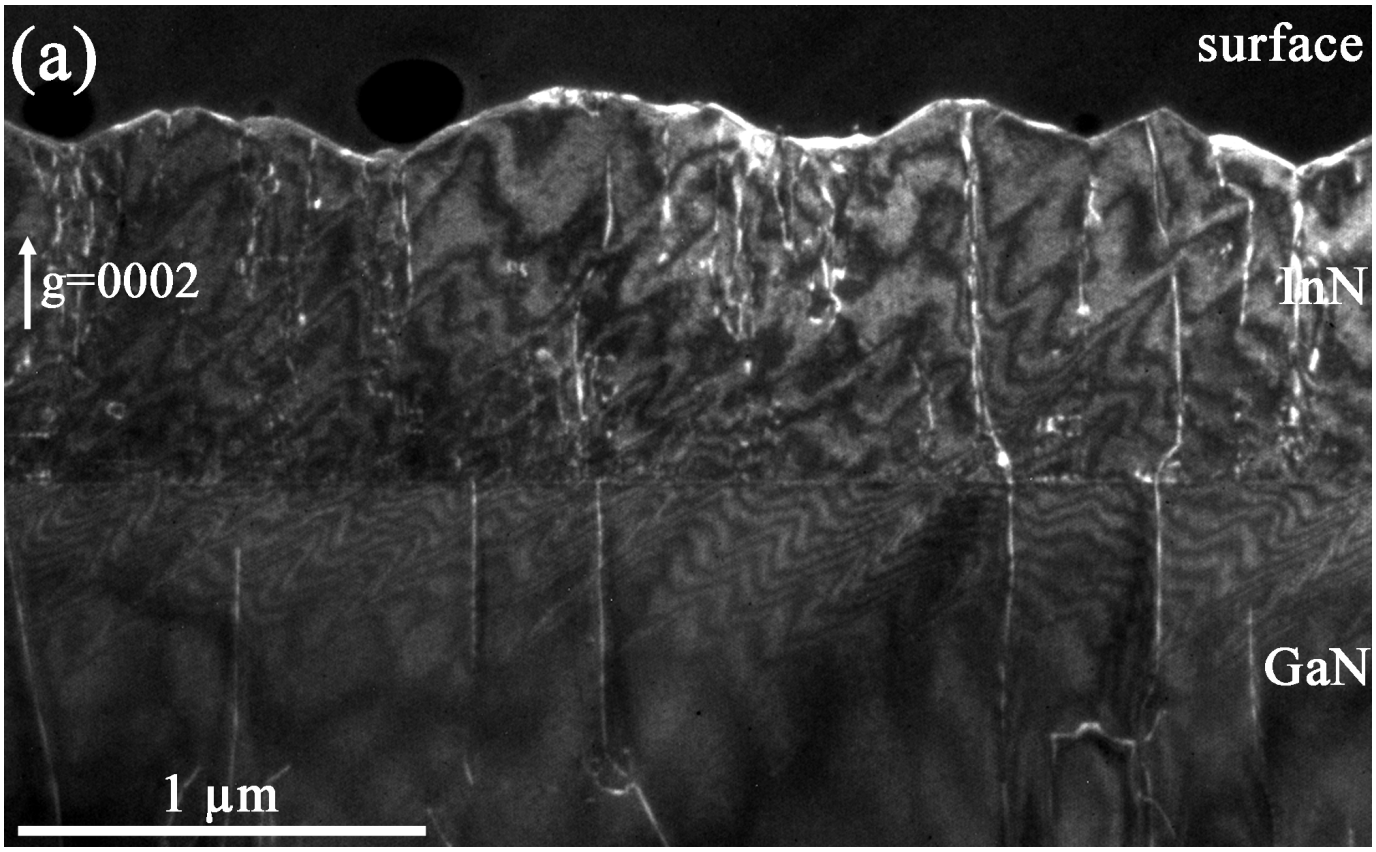

Figure 1a (Figure1a.tif)

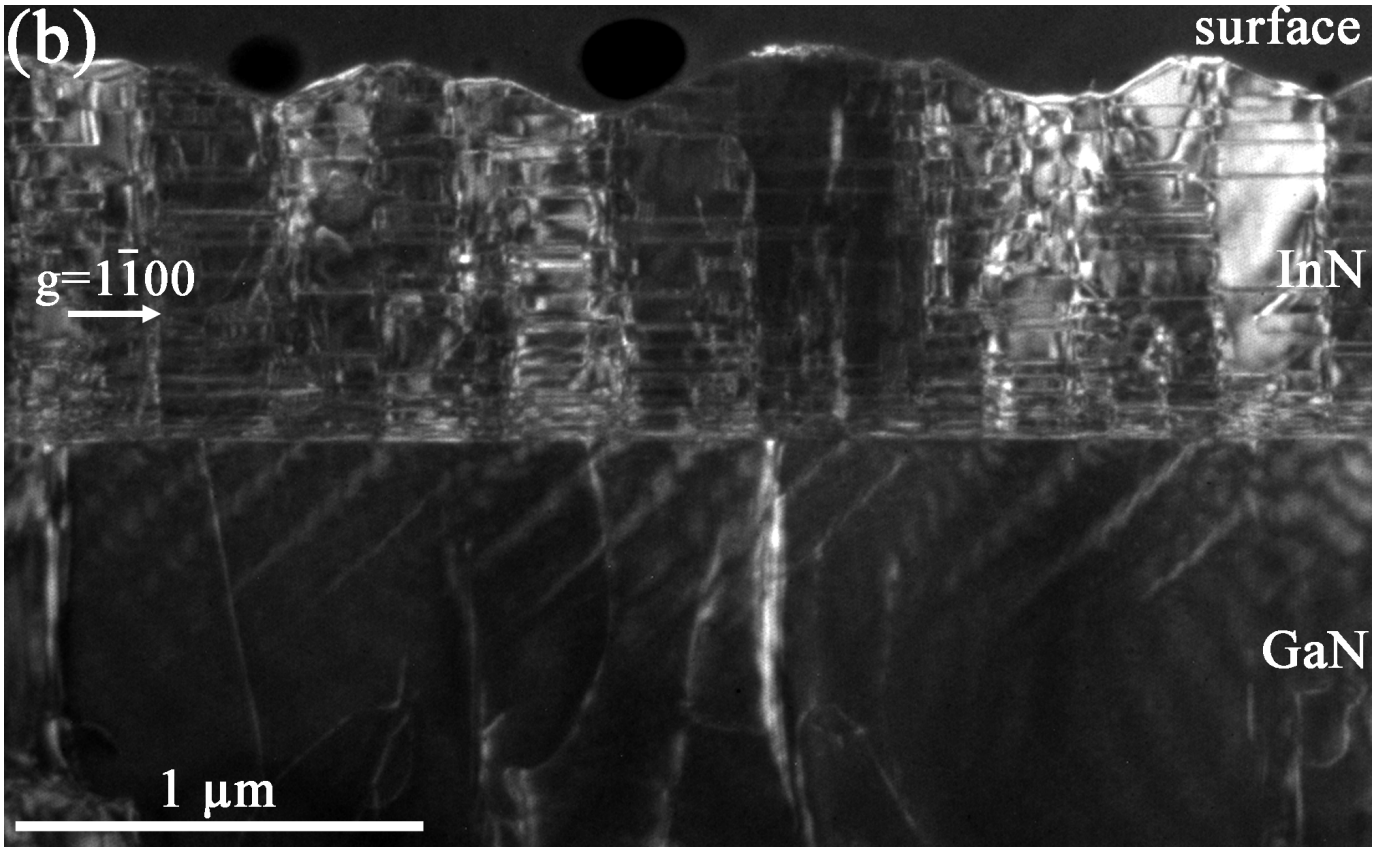

Figure 1b (Figure1b.tif)

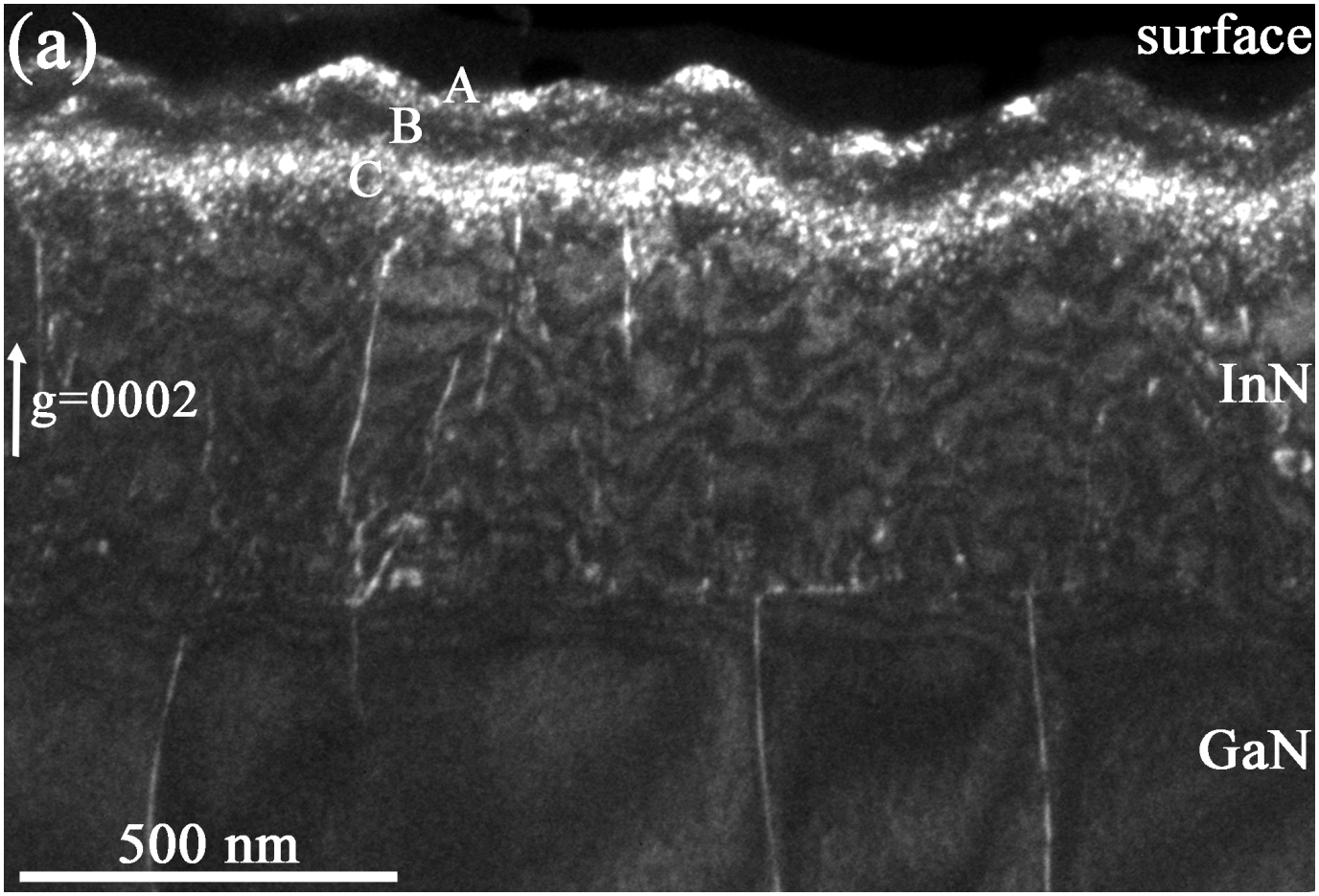

Figure 2a (Figure2a.tif)

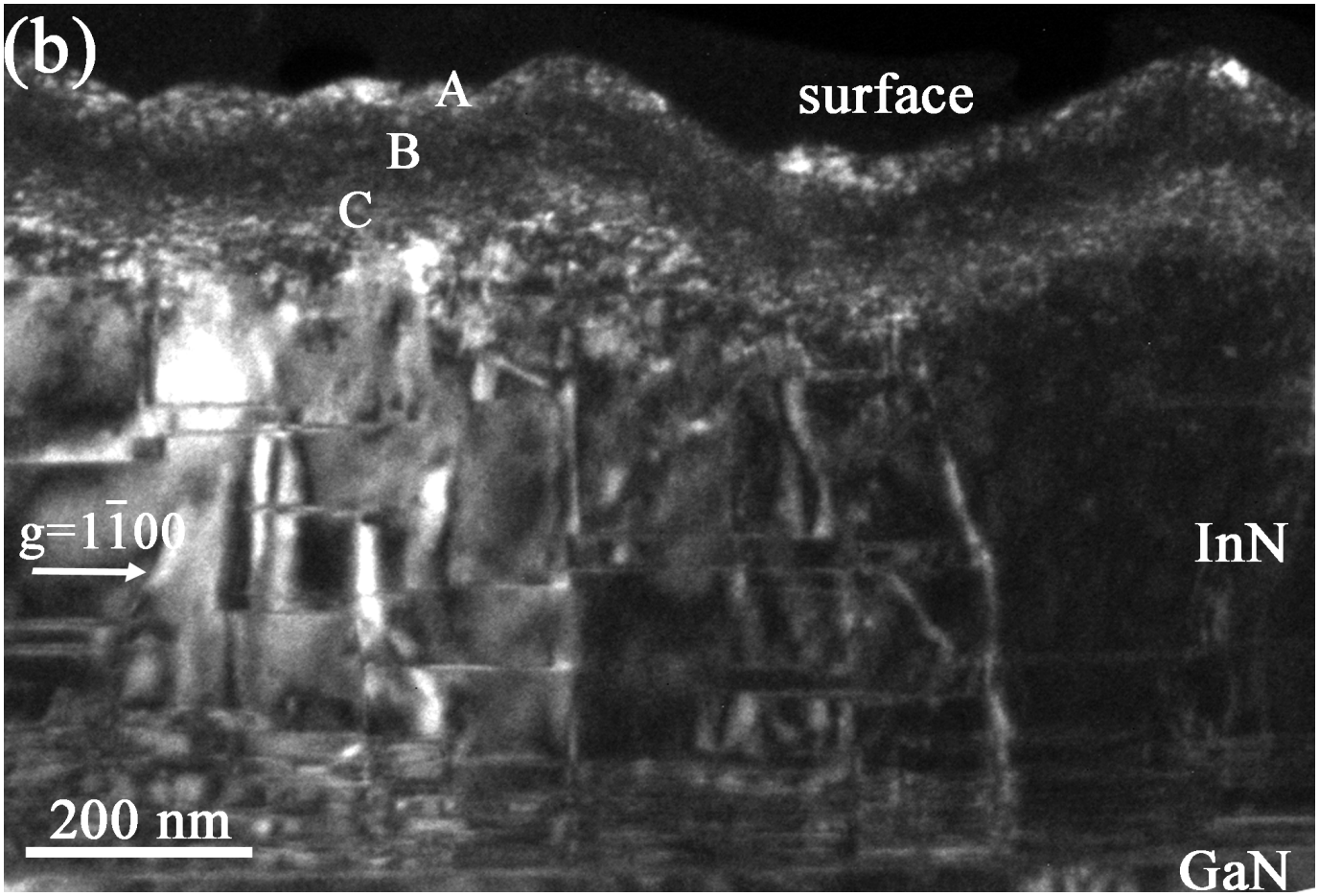

Figure 2b (Figure2b.tif)

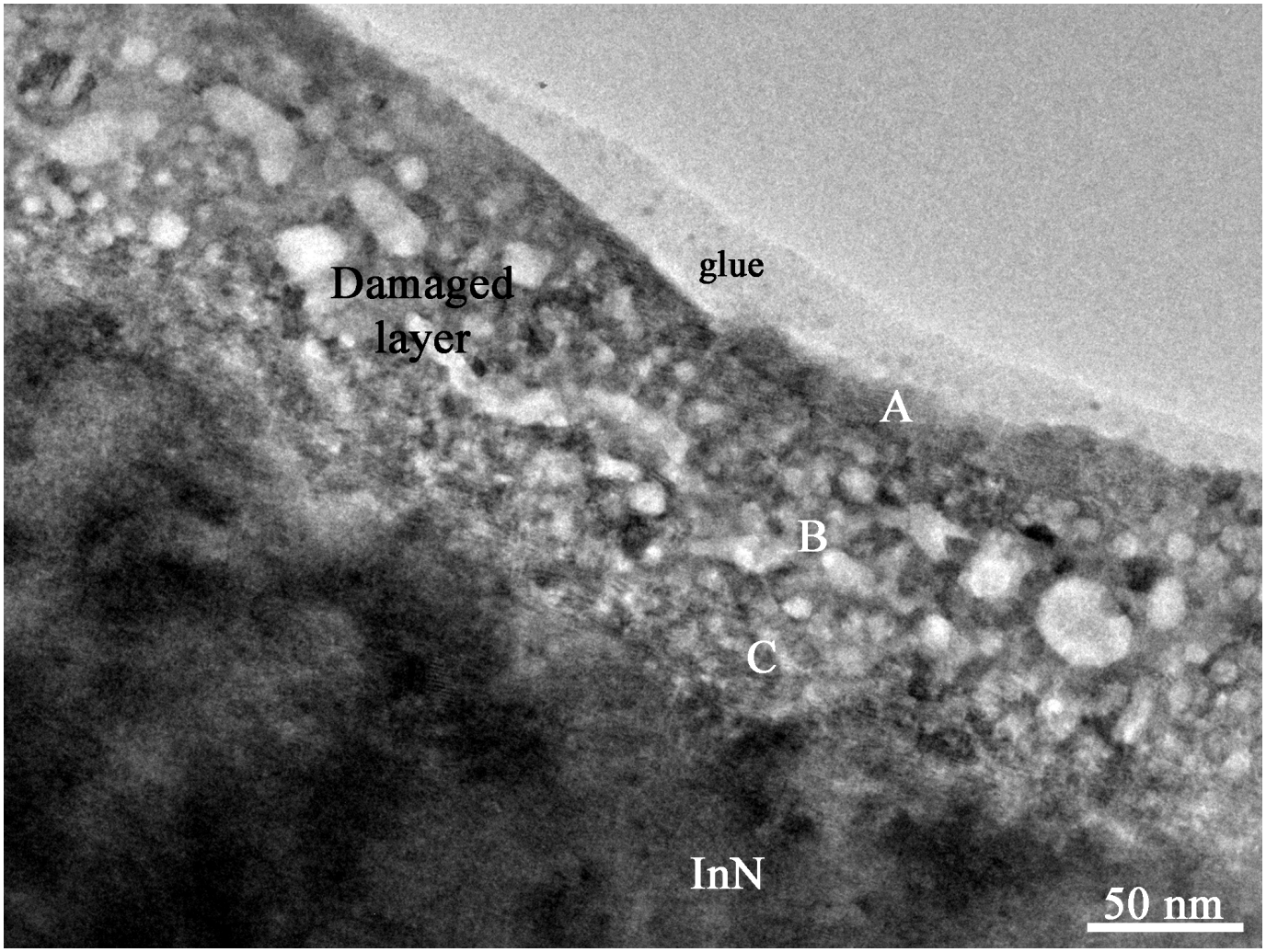

Figure 3 (Figure3.tif)

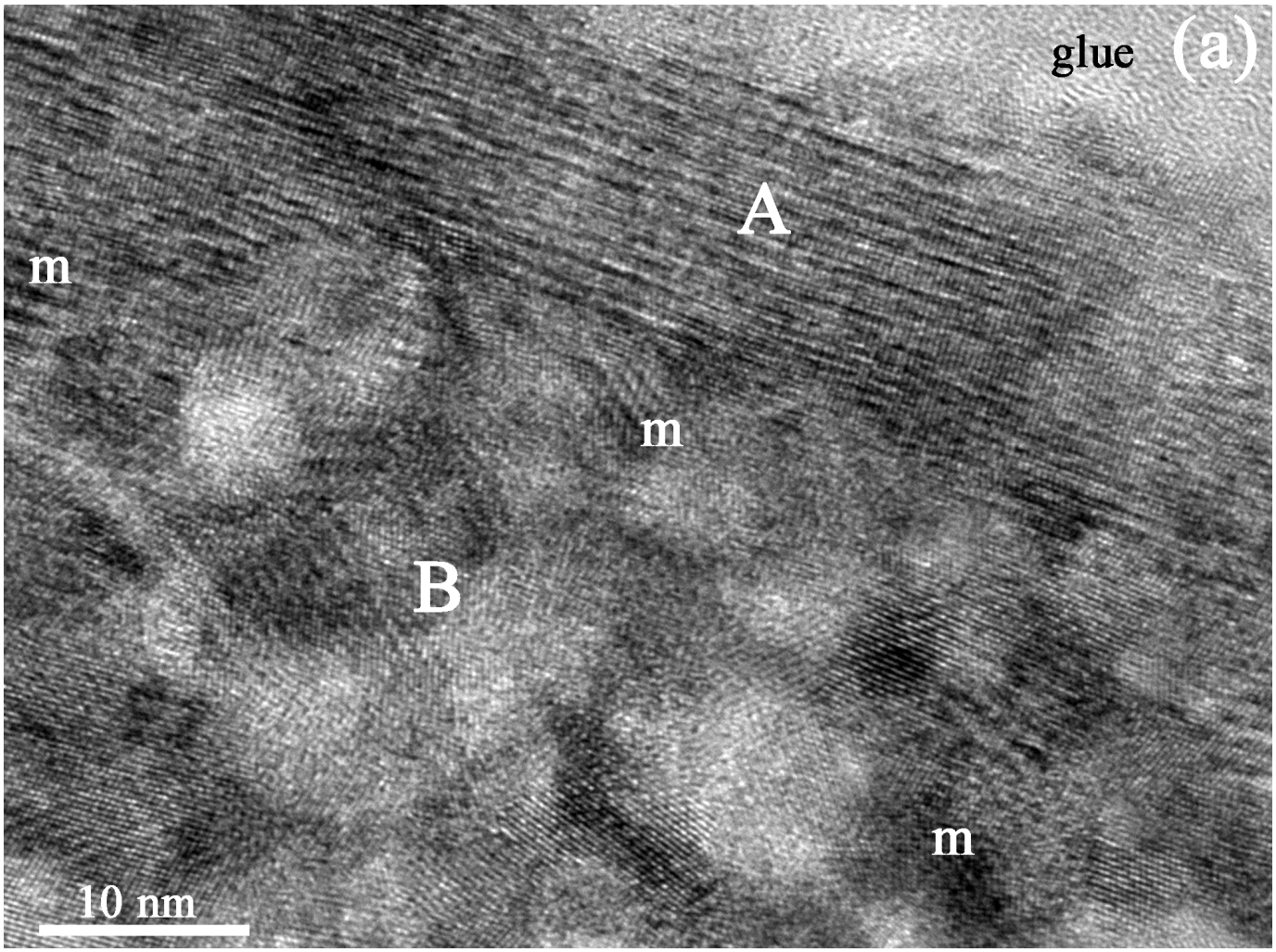

Figure 4a (Figure4a.tif)

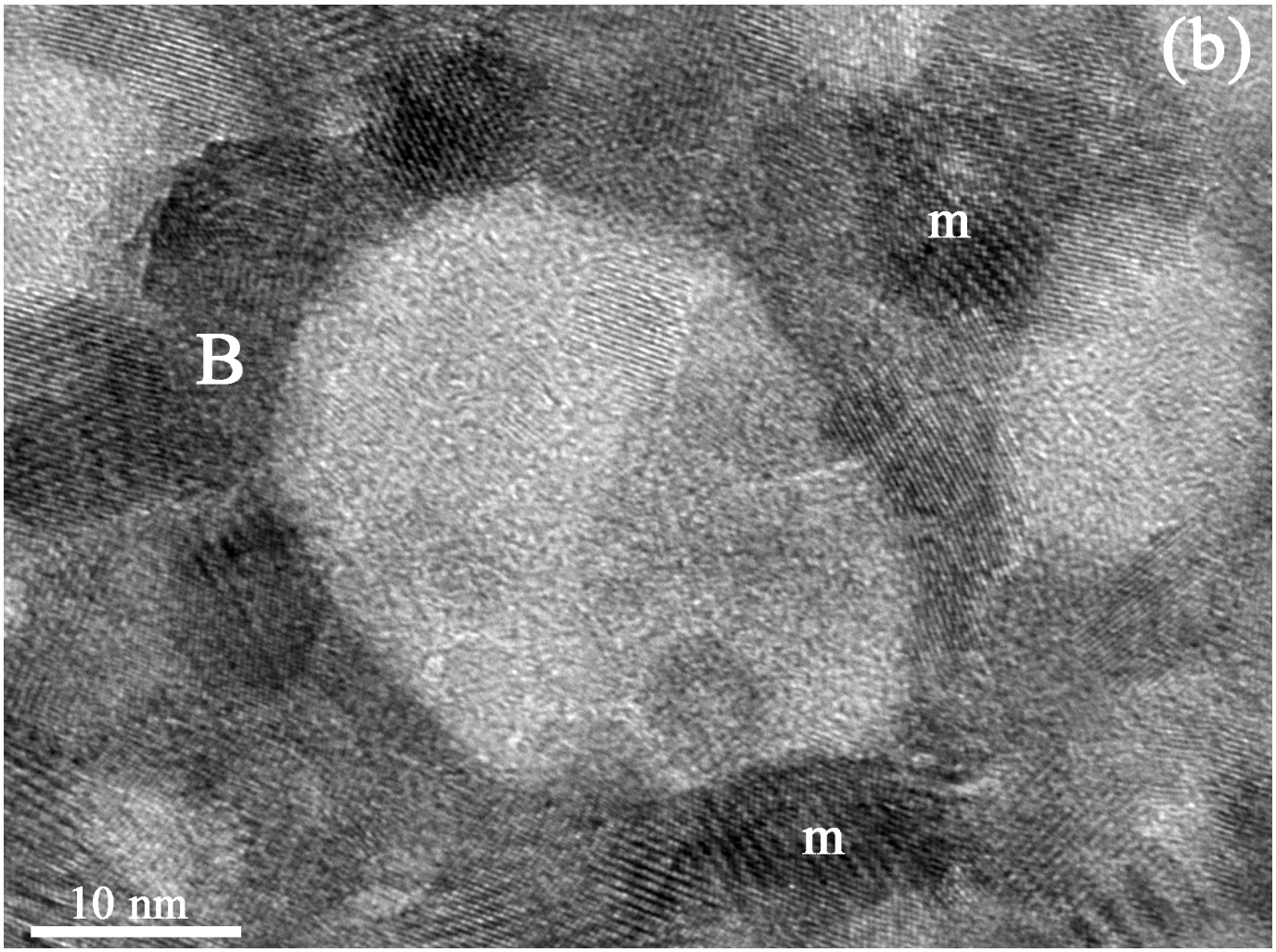

Figure 4b (Figure4b.tif)

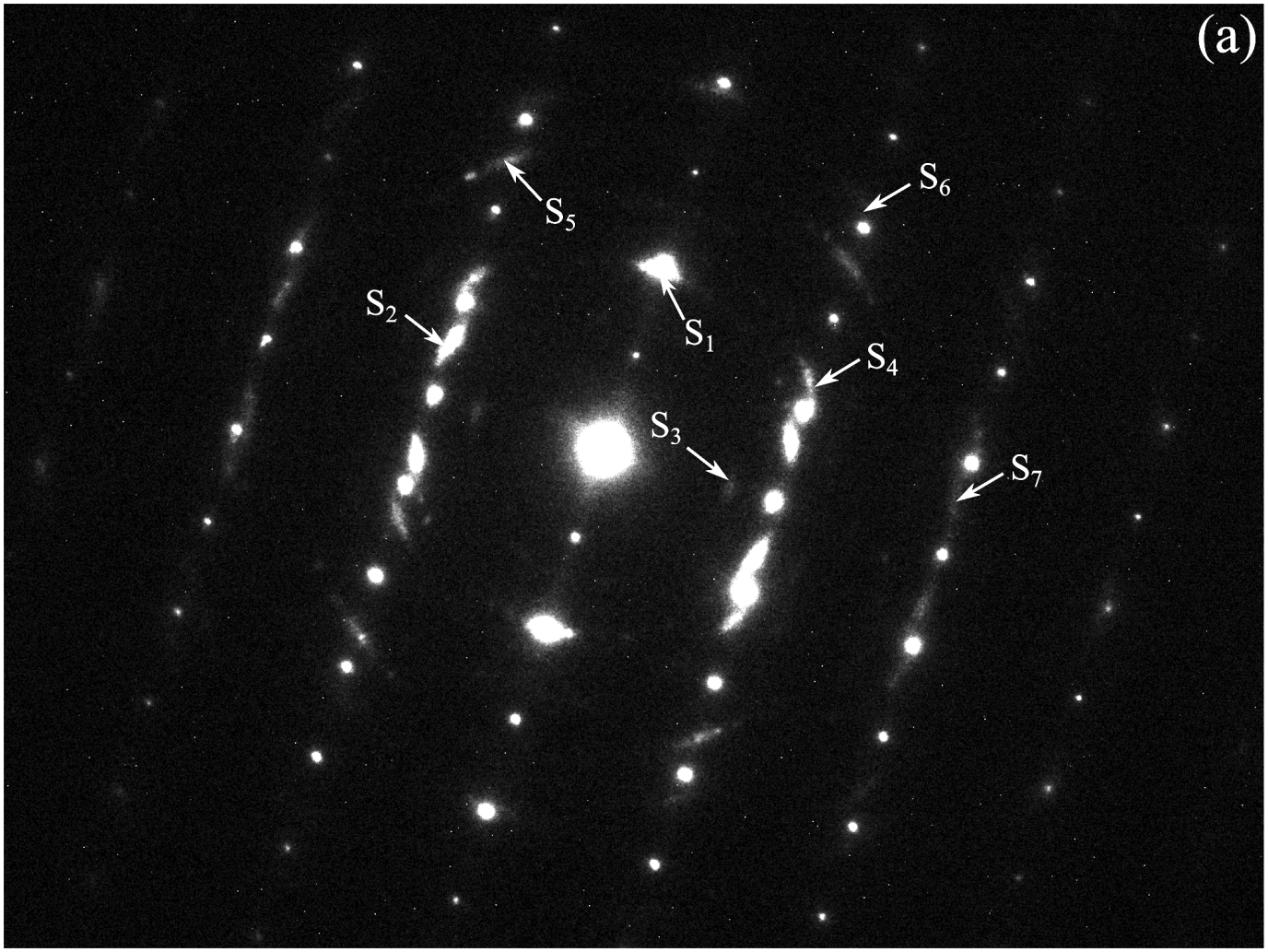

Figure 5a (Figure5a.tif)

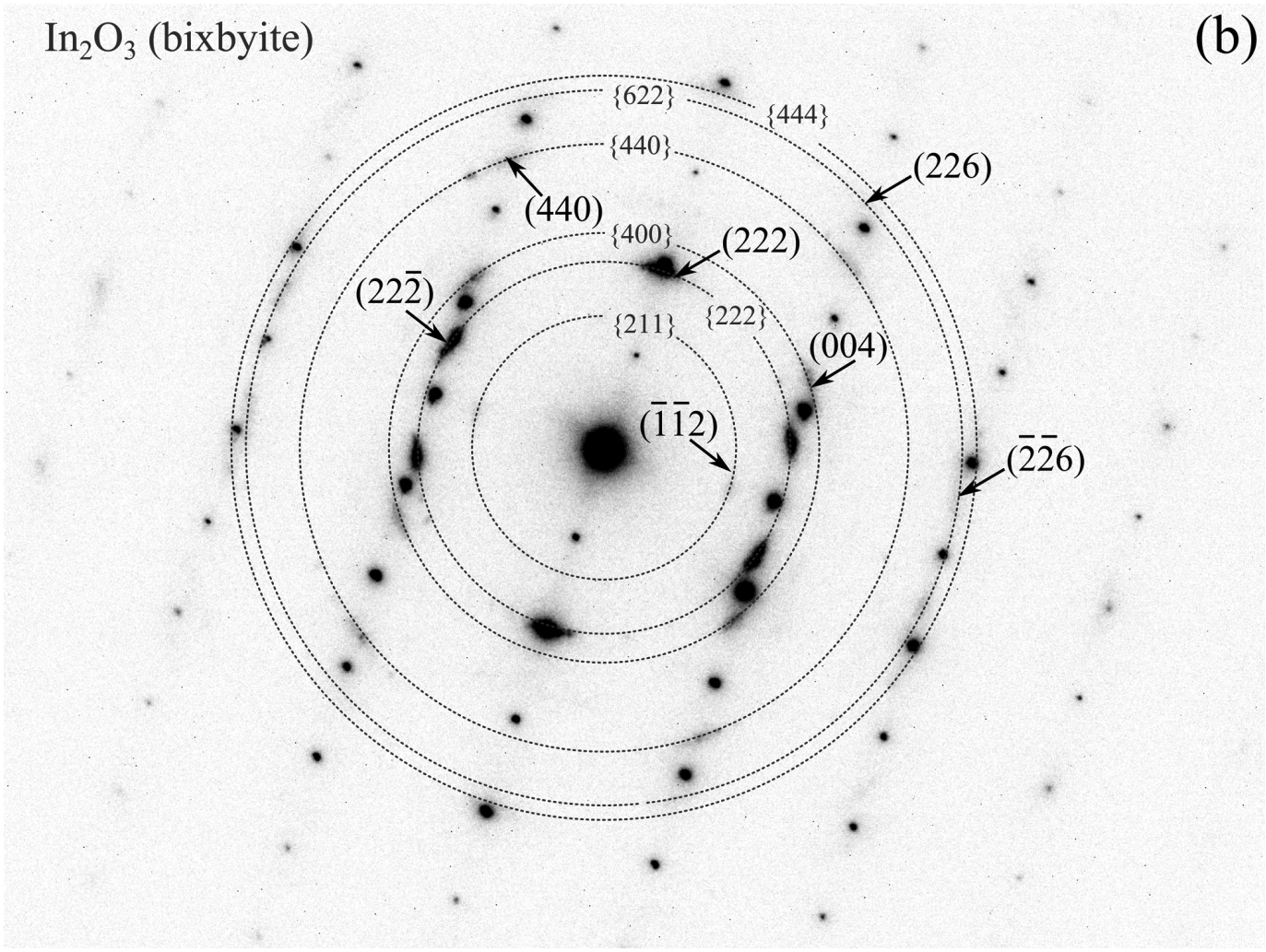

Figure 5b (Figure5b.tif)